LAWRENCE
LIVERMORE
NATIONAL
LABORATORY

LLNL-JRNL-405205

Benchmarking the x-ray phase contrast imaging for ICF DT ice characterization using roughened surrogates

E. Dewald, B. Kozioziemski, J. Moody, J. Koch, E. Mapoles, R. Montesanti, K. Youngblood, S. Letts, A. Nikroo, J. Sater, J. Atherton

July 8, 2008

Fusion Science and Technology

Disclaimer

Benchmarking the x-ray phase contrast imaging for ICF DT ice characterization using roughened surrogates

E. Dewald, B. Kozioziemski, J. Moody, J. Koch, E. Mapoles, R. Montesanti,
K. Youngblood, S. Letts, A. Nikroo, J. Sater and J. Atherton

Abstract
We use x-ray phase contrast imaging to characterize the inner surface roughness of DT ice layers in capsules planned for future ignition experiments. It is therefore important to quantify how well the x-ray data correlates with the actual ice roughness. We benchmarked the accuracy of our system using surrogates with fabricated roughness characterized with high precision standard techniques. Cylindrical artifacts with azimuthally uniform sinusoidal perturbations with 100 um period and 1 um amplitude demonstrated 0.02 um accuracy limited by the resolution of the imager and the source size of our phase contrast system. Spherical surrogates with random roughness close to that required for the DT ice for a successful ignition experiment were used to correlate the actual surface roughness to that obtained from the x-ray measurements. When comparing average power spectra of individual measurements, the accuracy mode number limits of the x-ray phase contrast system benchmarked against surface characterization performed by Atomic Force Microscopy are 60 and 90 for surrogates smoother and rougher than the required roughness for the ice. These agreement mode number limits are >100 when comparing matching individual measurements. We will discuss the implications for interpreting DT ice roughness data derived from phase-contrast x-ray imaging.
*This work performed under the auspices of the U.S. Department of Energy by Lawrence Livermore National Laboratory under Contract DE-AC52-07NA27344

I. INTRODUCTION

In indirect drive ignition experiments planned for the National Ignition Facility [1], 192 351 nm wavelength laser beams with a total energy of 1.2 MJ will heat the interior of a high-Z hohlraum to generate soft x-rays. The x-rays compress a 2-mm diameter, 100-um thick capsule that is placed inside the hohlraum and contains a 100 um thick deuterium-tritium (DT) fuel ice layer. According to hydrodynamic simulations [1], the interface between the DT ice layer and gaseous DT core in an ignition capsule has to meet certain maximum roughness requirements for successful fuel compression and subsequent ignition and burn.

We use x-ray phase contrast imaging [2] and optical shadowgraphy [3] to characterize the uniformity and surface roughness of our DT layers inside ignition capsules. While optical shadowgraphy can be used only for optically transparent ablators, x-ray phase contrast imaging is the only method that can be used for ice roughness measurements in the Be baseline capsule. Being a radiography technique, x-ray phase contrast imaging has an inherent integration over some target thickness that will result in smoothing of the high modes of the roughness power spectra. Other differences between inferred and actual ice surface roughness are possible, and while these can be modeled they have not previously been characterized experimentally.

As a step in this direction, we fabricated roughened artifacts to correlate phase contrast results with actual roughness that is pre-characterized using alternative high precision methods. We developed two types of artifacts. The first type consists of CH cylinders with an azimuthally uniform perturbation, and benchmarks the limits of our x-ray imaging system without the smoothing effect due to a random roughness that occurs in the case of the spherical DT layer. The second type consists of spherical PAMS beads [4] with a random roughness similar to that expected from a DT ice layer [1]. We measure the roughness of the beads with phase-contrast imaging before and after the beads were coated with a plastic layer that serves to approximate the refractive index jump between DT ice and DT gas.

II. THE X-RAY PHASE CONTRAST SYSTEM

All x-ray phase contrast tests using artifacts were performed in a setup that is similar to that used for the actual DT layer characterization [2], shown in Figure 1.

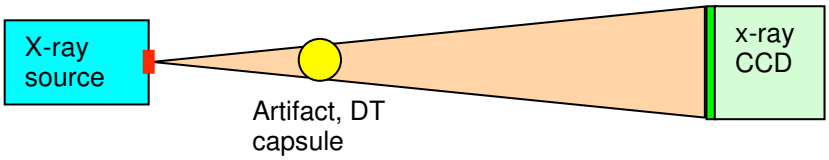

Fig. 1. Layout of the x-ray phase contrast system.

The set-up is a high magnification (10x), point-projection arrangement with a source-to-CCD distance of 100 cm. Our x-ray source is a micro-focus Kevex tube with a W transmission anode, typically operated at 50 kV voltage with a power of 4 W. In this operation mode, the source emits mainly L-shell radiation of W near 8.4 keV. We characterized the source spot size using the same geometry and a highly opaque spherical object and found a FWHM of 4 um.

Our detector is a 16 bit Princeton Instruments x-ray CCD camera with 1300x1000 pixels and 20x20 um pixel size. We increase the photon statistics in our analysis by aligning and overlapping 80-150 individual x-ray images.

III. CYLINDERS WITH AZIMUTHALLY UNIFORM PERTURBATIONS

Polystyrene cylinders with a diameter of 2 mm were diamond machined to create azimuthally symmetric sinusoidal perturbation along the axis, as shown in Figure 2.

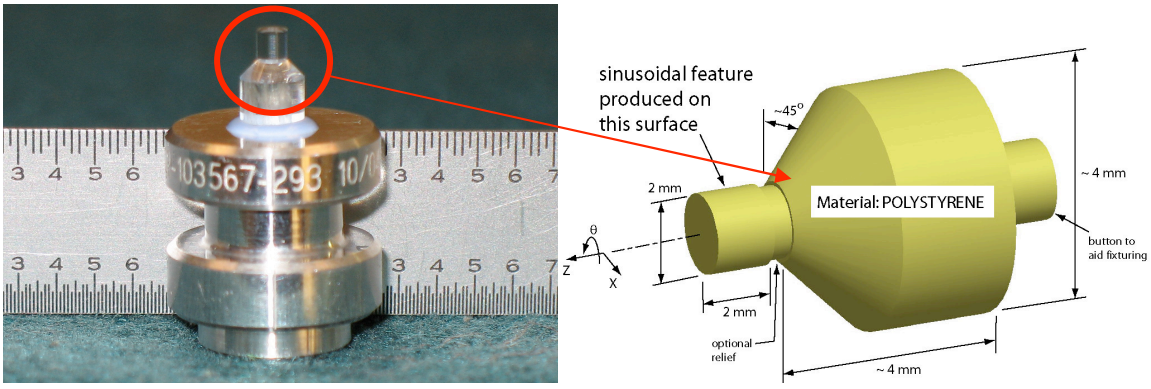

Fig 2. Photograph and schematics of cylindrical artifact with azimuthally uniform perturbations.

The artifact metrologized using a Zygo optical profilometer [5], and revealed a perturbation peak-to-valley amplitude of 0.974 um with a spatial period along the axis of 100 um. The cylindrical artifact was then characterized with our x-ray phase contrast system in the set-up shown in Fig. 1. Figure 3 shows x-ray radiography data of the artifact obtained by overlapping 150 individual images to increase the signal-to-noise ratio.

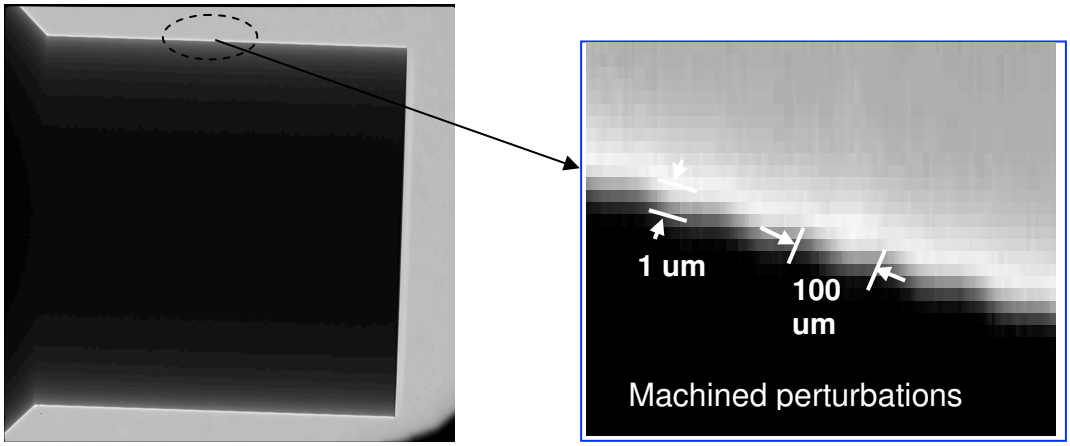

Fig 3. X-ray phase contrast image of the cylindrical artifact.

The perturbation countour tracing obtained by profilometry is compared to the x-ray phase contrast data, and the results are summarized in Figure 4 together with the corresponding sinusoidal fits. Very good agreement was found between the profilometer and x-ray phase contrast data. The sine fits to experimental data revealed an amplitude of 0.47 um for radiography and 0.487 um for profilometry. This result shows that the deviation between the two methods is considerably smaller than the resolution of the x-ray phase contrast setup limited mainly by the source size (4 um in the object plane). The reason for this is that the perturbation amplitude is measured over 100 um period that consists of several resolution elements.

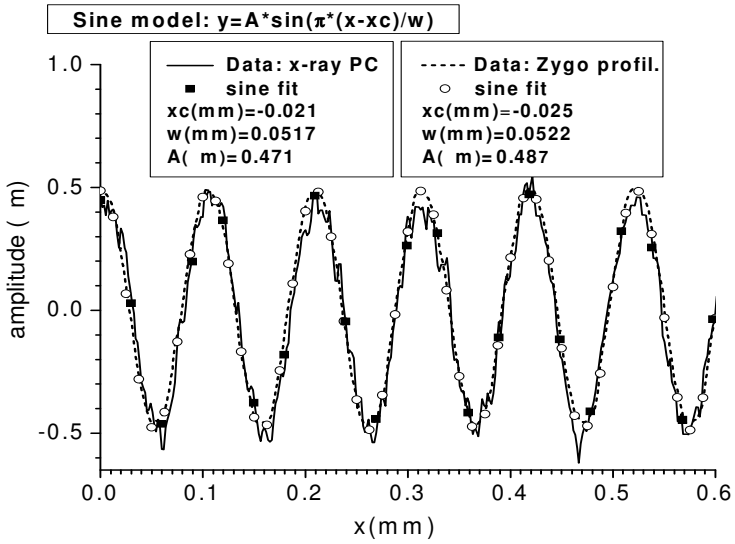

Fig. 4 Comparison of cylindrical artifact perturbation data obtained with profilometry and x-ray phase contrast system.

This result demonstrates the high precision of phase contrast imaging system in the absence of random roughness smoothing.

IV. SPHERICAL SURROGATES WITH RANDOM ROUGHNESS

A) Fabrication of artifacts and their roughness characterization by Atomic Force Microscopy (AFM) spheremapping

Artifacts with random roughness, similar to what we expect in a DT layer, were developed to benchmark the accuracy of our phase contrast limit in conditions that are similar to the DT ice layer characterization. These artifacts consist of spherical PAMS beads with a diameter of 1.7 mm, roughened using various methods. In our surrogate roughening we aimed for surface characteristics and power spectra that are similar to those required for a DT layer-gas interface in a 2 mm Be capsule for successful ignition, according to complex hydrodynamic calculations [1]. A roughness slightly lower than required was obtained by sand paper roughening over a duration of 6 minutes, while a roughness slightly higher was obtained by bead roughening in a sonic bath over a duration of 48 hours.

The surface roughness of the artifacts was characterized by Atomic Force Microscopy (AFM) spheremapping [6]. We performed 12 individual roughness measurements performed within a waistband area with a width of 150 um from which we generate power spectra. The same specific area chosen for the AFM measurements is then characterized by x-ray phase contrast imaging. The average of the 12 power spectra for the smooth and rough surrogates shown in Fig. 5 “encapsulate” the ignition specifications, also shown on the plot, within a factor of 10 at mode numbers of ~60. We roughened several PAMS beads using these two methods and the artifacts roughened with the same method show similar power spectra.

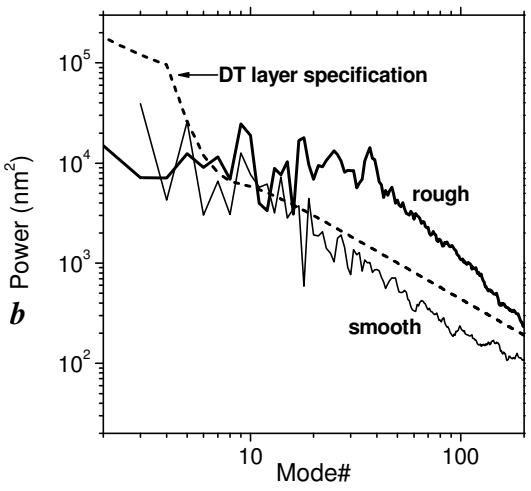

Fig. 5. Average power spectra of 12 invididual AFM measurements for the randomly roughened PAMS bead artifacts that are similar to the DT layer roughness specification.

B) Artifact characterization by x-ray phase contrast imaging

After centering the PAMS bead in the AFM system, we applied a glue dot on the artifact to ensure that the same area that was characterized by AFM is measured by our x-ray phase contrast system as shown in Figure 6. The glue was mixed with metallic powder to enhance its contrast due to x-ray absorption on the acquired radiographs.

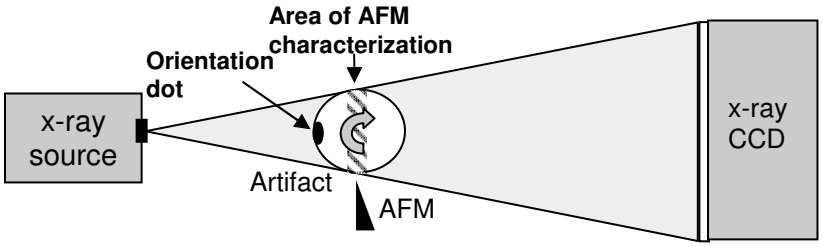

Fig. 6. Procedure used to compare x-ray phase contrast measurements with AFM data for the roughened surrogates.

We performed 7 independent x-ray measurements by rotating the surrogate with 5° steps within ±15° range from the centering glue dots as shown in Figure 6. Figure 7 shows typical radiographs for the rough and smooth surrogates obtained by overlapping 150 individual x-ray images. The surrogate rougher than specifications shows high-Z impurity dots that have contaminated the surface during the roughening process.

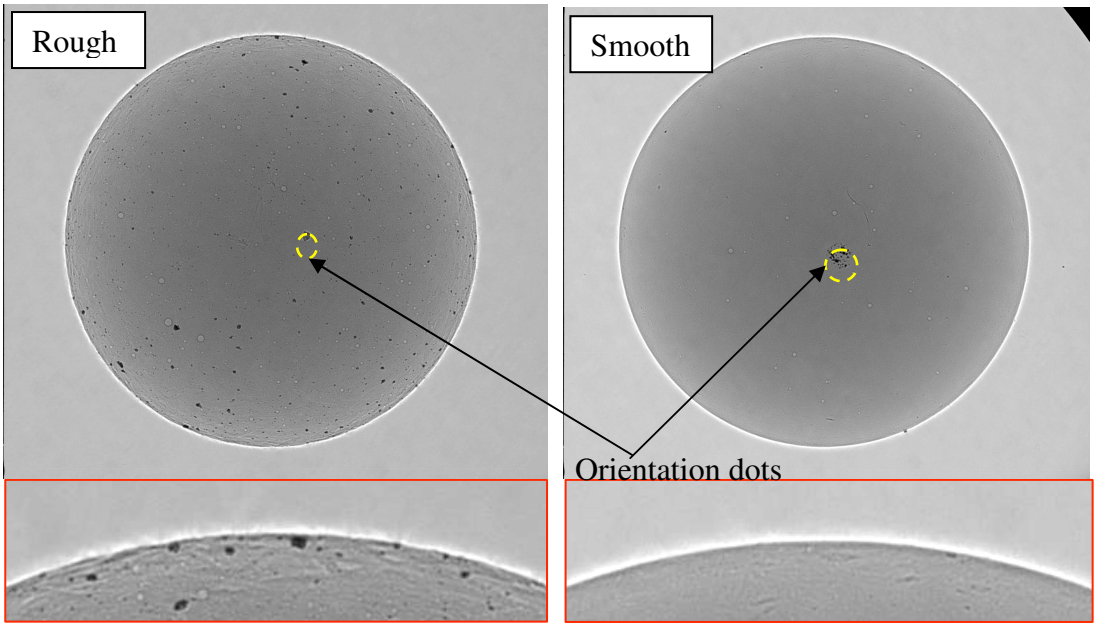

Fig. 7. Full phase contrast x-ray radiographs of PAMS surrogates with roughness lower and higher than specifications (Fig. 5) and magnified areas of these radiographs that show the difference in surface roughness.

The magnified areas show clearly that the limb of the rough surrogate has a higher roughness than the smooth one. For each of the two artifacts, the average of the 7 independent measurements (Fig. 7) was compared to the 12 trace average AFM data (Fig. 5). Figure 8 shows the average AFM and x-ray data for the two surrogates, as well as the DT layer specifications.

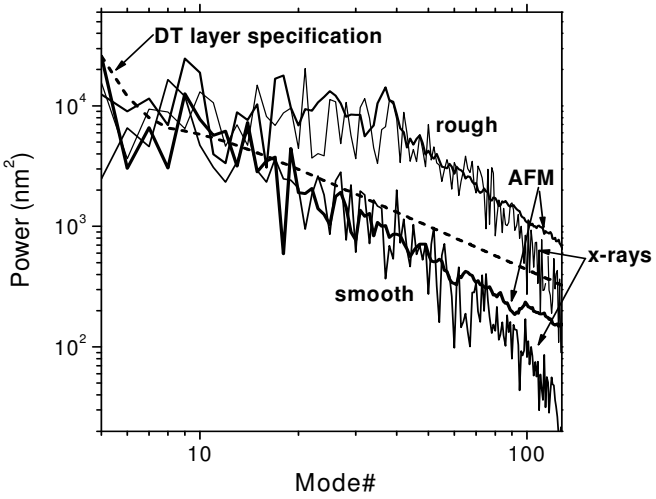

Fig. 8. AFM vs. x-ray phase contrast power spectra for the smooth and rough surrogates; DT layer specifications are also shown.

The x-ray phase contrast data for the two surrogates agrees with the AFM power spectra up to mode 60-90, after which the power spectra measured with phase contrast imaging is smoother than the actual (AFM) roughness. Specifically, considering an agreement limit given by the ratio between x-ray phase contrast and AFM power spectra of 0.8, the agreement limit mode number is 61 for the surrogate that is 2x smoother than the DT ice roughness specifications and 89 for the surrogate that is 3x rougher than the specifications. Overall this result shows that the characterization method reproduces the ice roughness at least up to mode 60.

C) Artifact coating and the corresponding x-ray phase contrast data

The surrogates were developed to simulate the roughness of the DT ice layer at its interface with the gaseous capsule fill. Since for good surrogacy of the DT ice layer we primarily have to match the refractive index ratio between the layer and gas fill, the next step in our benchmarking using surrogates was to identify a surrogate coating that would have refractive index ratio relative to the PAMS substrate material similar to the DT ice-to-gas. For the uncoated surrogate, the ratio between the refractive index of the environment and the uncoated surrogate interface is in fact smaller than 1, while for a coated surrogate the ratio would be larger than 1, similar to DT ice-gas interface. We identified CF_2 as being an acceptable coating to simulate the refractive index ratio at the ice surface of a DT capsule.

One of the main conditions for a successful coating, performed by chemical plasma deposition, was that the coating process had to be non-destructive for the applied PAMS surface roughness. Figure 9 shows a comparison of x-ray images and corresponding radial line-outs on the limb for the uncoated and coated surrogates as well for a DT layer in a Be capsule [8] measured with the same phase contrast setup (Fig. 1). There is a darker area that appears in the radiograph as centered on the stalk which has higher absorption and a few bubbles as a result on bead heating. In real space this is probably the closest area to the coating plasma stream and is on the opposite side to the stalk position. The images show, however, that the extent of this heated area does not affect the roughness measurements performed on the limb.

When comparing the images, one can see that the DT ice interface roughness as well as the bead-coating interface consist of dark bands, while the surface of the uncoated surrogate appears as a bright band. The reason for this is the unmatched air-surrogate refractive index ratio for the uncoated as compared to the DT-gas interface as mentioned above. This is shown quantitatively also by the radial line-outs performed on the limb area. The number of counts on the CCD shown in the line-outs demonstrate an increased x-ray absorption of the uncoated and coated surrogates compared to a DT layer due to the higher surrogate absorption than the combined absorption of the DT ice and Be shell.

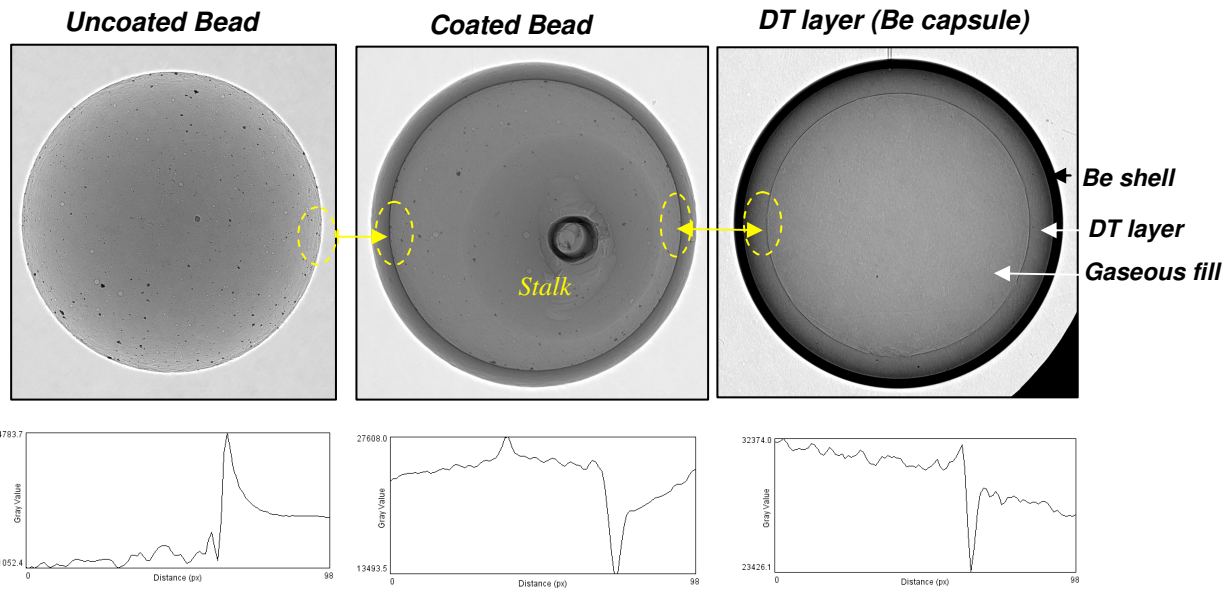

Fig. 9. Rough uncoated and optimally coated surrogates, DT layer in a Be shell and corresponding radial lineouts in the limb area.

The coated surrogate dark band reproduces qualitatively well the DT ice-gas interface. However, the width of the dark band (Fig. 9) is 2x larger in the surrogate case. According to [9] the width of the dark band *i* is given by:

$$i = 3\left(\frac{p+q}{p}\right)^{1/3}\left(q(n1-n2)\sqrt{R/2}\right)^{2/3} \qquad (1)$$

where p is the source-to-object distance, q is the object-to-detector distance, R is the object radius, n1is the refractive index of the PAMS surrogate or DT gas and n2 is the refractive index of the surrogate coating or DT ice. The refractive index for DT ice is n_{ice}=1-6.5e-7 and for DT gas n_{gas}=1-1.6e-9. For the coated surrogate, n_{bead}=1-3.8e-6 and for the CF_2 coating $n_{coating}$=1-5.7e-6. It follows that

$$n_{bead}\text{-}n_{coating}=2.92x(n_{gas}\text{-}n_{ice}) \qquad (2)$$

and consequently that, according to Eq.(1) $i_{surrogate}$=2.03x i_{ice} which is in quantitative agreement with the difference in the width of the dark bands of the coated surrogate and the DT ice layer observed experimentally (Fig. 9).

We compared the AFM data and x-ray data of the uncoated rough surrogate to the x-ray data of a coated surrogate that was roughened in the same batch and the result is shown in Figure 10. This comparison using surrogates from the same batch rather than the same surrogate can be performed since the power spectra of surrogates roughened in the same batch proved to be very similar.

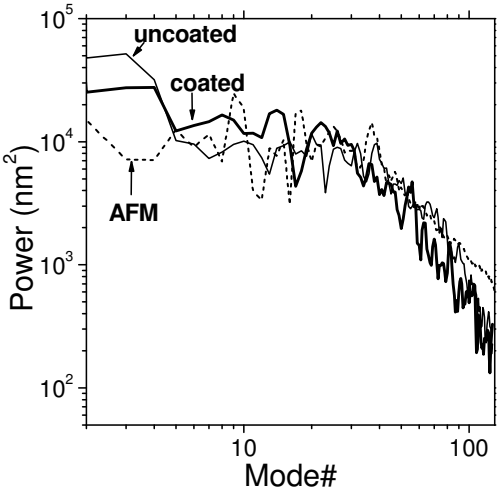

Fig. 10. Power spectra for the uncoated surrogate according to AFM measurements (black line), and from x-ray measurements (blue line), as well as for a coated surrogate from the same roughening batch measured by x-rays (red line)

The coated and uncoated surrogates with the same initial roughness show similar power spectra and both agree with the actual (AFM) roughness up to mode ~90. This shows that matching the refractive index ratio does not play an important role in the agreement between the actual roughness, i.e. the AFM data, and the x-ray phase contrast measurements.

D) Effect of power spectra averaging and error bar estimates

We have chosen to compare average power spectra for the two surrogates measured by AFM and x-ray phase contrast imaging due to the fact that it was not possible to align the surrogates in the AFM and radiography system precisely enough to measure the same surrogate contour. For this reason, for both methods, we performed independent measurements in roughly the same surrogate area and we averaged the resulting power spectra, after which we compared the average obtained from x-ray phase contrast to the AFM average. In consequence one source of error bars when benchmarking the x-ray phase contrast method against AFM is the deviation of the individual measurements from their averages.

For both methods we calculate the deviation of the individual measurements from the power spectra average as the standard error of the mean (SEM) defined as

$$SEM = \frac{SD}{\sqrt{n}} \qquad (3)$$

where n is the number of individual measurements and SD is the standard deviation defined as:

$$SD = \left[\frac{1}{(n-1)} \sum_{i=(0,n)} \left(X_i - \langle X \rangle \right)^2 \right]^{1/2} \qquad (4)$$

In this equation X_i is the individual power spectrum measurement i and <X> is the average of all n individual power spectra.

We apply this error analysis first to the x-ray phase contrast data and then to AFM surface characterization. We represent the deviation of the 7 individual x-ray measurements by plotting SEM [Eq. (3)] as error bars from their average and the results are shown in Figure 11a. Furthermore, the SEM is also shown as relative error from the average in Figure 11b. Interestingly, the relative deviation of the individual measurements from their average is similar for both rough and smooth surrogates. Moreover, this relative deviation varies across the entire power spectra about a constant value of 17%.

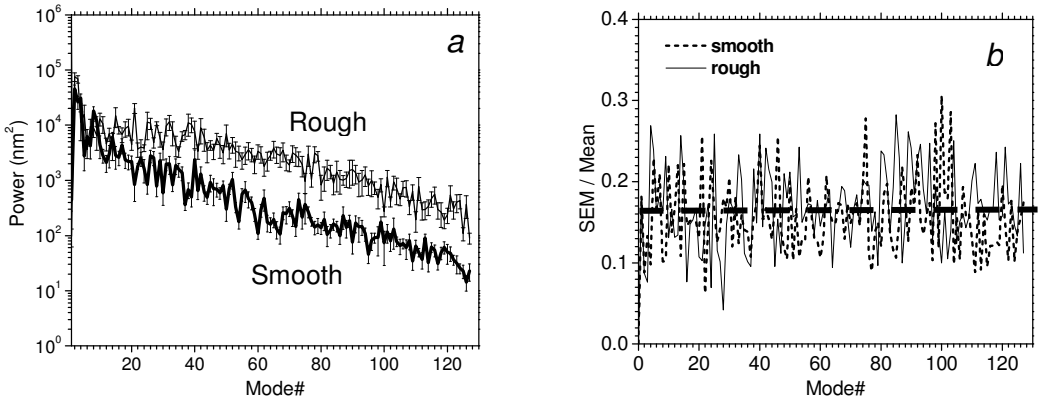

Fig. 11 Deviation of individual x-ray measurements from their average shown as (a) SEM error bars and (b) as relative error from the average for both surrogates.

We also compared the deviation of individual AFM measurements from their average and the results are summarized in Figure 12, similar to the x-ray data (Fig. 11). It is interesting to note that the deviation of the individual AFM measurements from their average is slightly higher than for the x-ray measurements.

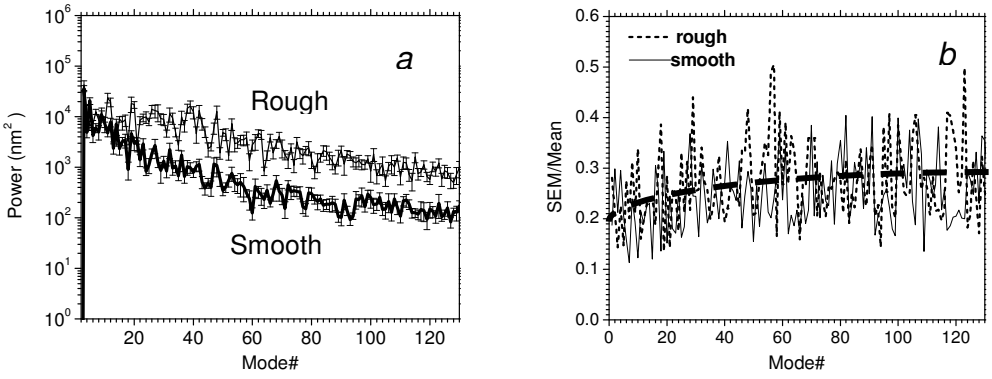

Fig. 12 Deviation of individual AFM measurements from their average shown as (a) SEM error bars and (b) as relative error from the average for both surrogates.

This is despite the fact that is the result of 12 individual AFM measurements rather than 7 in the case of x-ray phase contrast which should yield ~ 1.4 times lower SEM if the standard deviations are similar. Moreover, the average value of the relative error increases across the power spectrum from 20% at mode 1 to 30% at mode 127 as result of increasing noise contribution at high modes that have lower power (Fig. 12a). Similar to the x-ray measurements, the relative error is the same for both rough and smooth surrogates.

It is important to note that the estimated errors are mainly caused by the fact that each individual measurement probes a different contour of the surrogates. The reason we have chosen to compare averages of the AFM and x-ray data performed on separate contours rather than the same one is that it was not possible to center the same surrogate between the two different characterization methods to better than about 10 degrees. While the surrogates were developed with random, uniform roughness across their surface, roughness differences are present between individual measurements as clearly shown by the significant spread of the individual AFM data from their average (Fig. 12).

Since in our study we used surrogates roughened in the same batch when we looked at the coating effects on the x-ray measurements (Fig. 11), it is important to compare the roughness of individual beads within the same batch. Figure 13 shows the average power spectra and their corresponding deviations of the individual measurements (SEM) for two smooth and two rough surrogates prepared in the same batches.

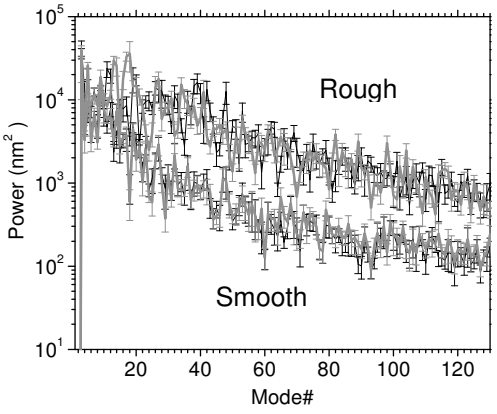

Fig. 13 Comparison of AFM average power spectra and corresponding SEM for two individual smooth and two rough surrogates created in the same batches (thin black and thick grey lines).

The power spectra for the different surrogates roughened in the same batch are very similar. Furthermore, the deviation of the average power spectra of different surrogates belonging to the same batch is smaller than the deviation of the individual measurements from their average for each surrogate. This allows us to compare the power spectra coated and uncoated surrogates roughened in the same batch (Fig. 10).

E) Deviation of individual x-ray measurements from individual AFM data

All individual AFM and x-ray measurements were performed within similar sections of the surrogate surfaces and until now we compared the average power spectra between these methods to relate the x-ray data to real surface roughness measured by AFM. Another approach to benchmark our x-ray phase contrast system is to compare individual x-ray measurements to individual AFM traces.

Figure 14 shows two samples for both measurements obtained for the rough and smooth surrogates. For both surrogates the AFM data show a large high mode variation that ranges from agreement with x-ray measurements as shown by the AFM 2 trace, to higher power than for the x-ray measurements at modes > 60-90 (AFM 1 trace), similar to the averages comparison (Fig. 8). For both surrogates, the AFM 2 data traces agree with the x-ray power spectra over a mode range >100.

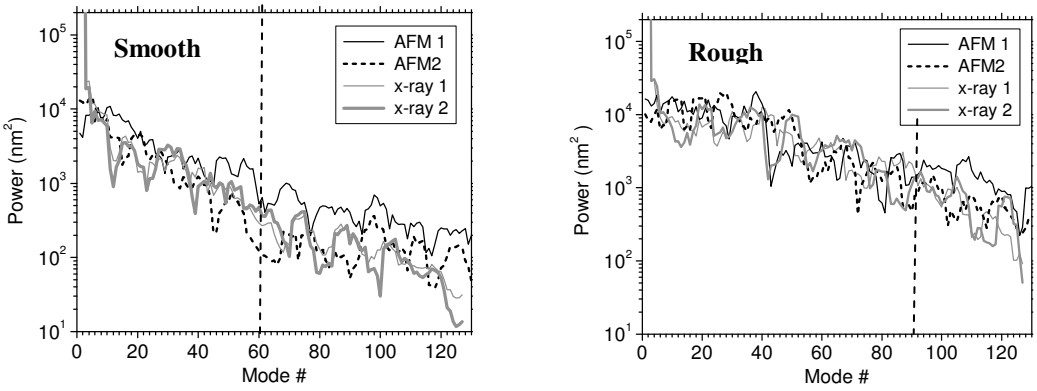

Fig. 14 Samples of individual power spectra from AFM (black lines) and x-ray (grey lines) measurements for both surrogates demonstrating large variation between individual AFM high mode data; the dashed line shows the agreement limits obtained using the averages (Fig. 8).

The power spectra from x-ray measurements are similar over the entire mode range. This shows that the agreement mode limits between the average x-ray and AFM measurements (Fig. 8) may be caused by the large variations of the AFM power spectra. This means that, for surface roughness in the order of the DT layer specification for ignition, x-ray phase contrast may faithfully reproduce actual roughness to modes up to and beyond 100.

V. SUMMARY

We have benchmarked the x-ray phase contrast system used to characterize DT ice roughness in ignition capsules. The measurement limit of the system due to source size and x-ray CCD pixel size was characterized using a cylindrical artifact with azimuthally uniform perturbations with a peak-to-valley amplitude of 1 um and a 100 um period. The x-ray phase contrast data shows 17 nm deviation from the surface characterization results performed with a Zygo profilometer, which is considerably better than the limits due to source (4 um) and CCD pixel size (22 um).

We have fabricated two roughened PAMS beads with random roughness that encapsulate the required DT ice roughness specifications within a factor of 10. The surface roughness

was characterized with AFM. Due to the inherent imprecision of alignment of these beads in the AFM and x-ray phase contrast system, the power spectra were averaged over 12 AFM traces within a 150 um waistband. The results were compared with the average of 7 power spectra obtained from x-ray measurements performed by rotating the beads in 5 deg. steps about the same waistband. The average x-ray power spectra agree with AFM average spectra up to mode 60 for the smoother surrogate and up to mode 90 for the rougher surrogate than DT layer specifications.

We have coated the surrogates to match the refractive index ratio between DT ice and gaseous fill of the fuel capsule and the agreement limits of the x-ray phase contrast spectra with the AFM data are similar to the uncoated ones. Line-outs in the limb area demonstrate that the coated surrogates reproduce qualitatively the dark band between the ice and gaseous fill, with a wider dark band for the surrogate than for ice. The difference in the width of the dark band can be explained by the difference in refractive indexes for the DT ice and surrogates.

The deviation of the individual power spectra from their averages are represented as standard error of the mean SEM. For x-ray phase contrast, the deviation of the individual measurements from their average varies about a constant value of 17% across the power spectra for both surrogates. For AFM, however, this deviation increases from 20% at low modes to 30% at high modes, for both surrogates.

If we choose to compare individual x-ray measurements with individual AFM traces, the closest x-ray and AFM power spectra show agreement up to modes greater than 100. It seems that the agreement limits between phase contrast and AFM averages are mainly caused by the large deviation in the individual AFM traces, and x-ray phase contrast measurements may faithfully reproduce the actual surface power spectra for modes up to or exceeding 100.

References

[1] J.D. Lindl, Phys. Plasmas **2**, 3933 (1995); J.D. Lindl, P. Amendt, R.L. Berger, S.G. Glendinning, S.H. Glenzer, S.W. Haan, R.L. Kauffman, O.L. Landen, L.J. Suter, Phys. Plasmas **11**, 339 (2004).

[2] D.S. Montgomery, A. Nobile, P.J. Walsh, *Rev. Sci. Instrum*. **75**, 3987, 2004.

[3] J.A. Koch, T.P. Bernat, G.W. Collins, B.A. Hammel, B.J. Kozioziemski, A.J. MacKinnon, J.D. Sater, D.N. Bittner, and Y. Lee, *Fusion Technol.*, **38**, 123 (2000).

[4] R. Cook, S.R. Buckley, E. Fearon, S.A. Letts, *Fusion Technol.,* **35**, 206 (1999).

[5] L. Deck, P. de Groot, *Int. Journ. of Machine Tools and Manufacture,* **35**, 147 (1995).

[6] R.C. Cook, R. Mceachern, R.B. Stephens*, Fusion Technol.* **35***,* 224 (1999).

[7] D. Smith*, Thin-Film Deposition: Principles and Practice,* MacGraw-Hill (1995).

[8] B.J. Kozioziemski, J.D. Sater, J.D. Moody, J.J. Sanchez, R.A. London, A. Barty, H.E. Martz, D.S. Montgomery, *J. Appl. Phys.*, **98**, 103105 (2005).

[9] O.L. Landen, "Refraction Enhanced Imaging from Curved Interfaces", *LLNL internal memorandum, UCRL-MI-204761, 2004*.